Pre-print of a published manuscript

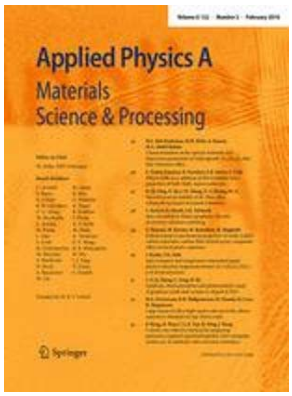

Formation of laser-induced periodic surface structures (LIPSS) on tool steel by multiple picosecond laser pulses of different polarizations

Peter Gregorčič, Marko Sedlaček, Bojan Podgornik, Jürgen Reif

DOI: https://doi.org/10.1016/j.apsusc.2016.06.174
Published in: Applied Surface Science, Volume 387, 30 November 2016, Pages 698-706

Received: 24 February 2016
Accepted: 28 June 2016

This is a pre-print of an article published in Applied Surface Science. The final authenticated version is available online at: https://doi.org/10.1016/j.apsusc.2016.06.174.

Please cite this article as: P. Gregorčič, M. Sedlaček, B. Podgornik, J. Reif, Formation of laser-induced periodic surface structures (LIPSS) on tool steel by multiple picosecond laser pulses of different polarizations, Appl. Surf. Sci., 387 (2016) 698-706, DOI: https://doi.org/10.1016/j.apsusc.2016.06.174

Formation of laser-induced periodic surface structures (LIPSS) on tool steel by multiple picosecond laser pulses of different polarizations

Peter Gregorčič[1]*, Marko Sedlaček[2], Bojan Podgornik[2], and Jürgen Reif[3]

[1]*Faculty of Mechanical Engineering, University of Ljubljana, Aškerčeva 6, 1000 Ljubljana, Slovenia*
[2]*Institute of Metals and Technology, Lepi pot 11, 1000 Ljubljana, Slovenia*
[3]*Brandenburgische Technische Universitaet – BTU Cottbus-Senftenberg, Platz der Deutschen Einheit 1, 03046 Cottbus, Germany*

*peter.gregorcic@fs.uni-lj.si, +386 1 477 1 172

Abstract

Laser-induced periodic surface structures (LIPSS) are produced on cold work tool steel by irradiation with a low number of picosecond laser pulses. As expected, the ripples, with a period of about 90 % of the laser wavelength, are oriented perpendicular to the laser polarization. Subsequent irradiation with the polarization rotated by 45° or 90° results in a corresponding rotation of the ripples. This is visible already with the first pulse and becomes almost complete – erasing the previous orientation – after as few as three pulses. The phenomenon is not only observed for single-spot irradiation but also for writing long coherent traces. The experimental results strongly defy the role of surface plasmon-polaritons as the predominant key to LIPSS formation.

Keywords: LIPSS; self-organization model; laser microprocessing

1 Introduction

Laser-induced periodic surface structures (LIPSS) have been intensively studied on different materials in the last half of the century [1-8]. They can be observed in all kinds of solids, when irradiated near their ablation threshold [9]. LIPSS appear as a regular ripple structure with a period that often scales with the laser wavelength [5], while its orientation and shape is defined by the polarization of the incident light [10, 11]. Since surface morphology is a key factor in controlling the optical, mechanical or chemical properties of a solid surface, laser-induced surface modification found great interest in a wide range of different applications in photonics, biomedicine, heat transfer, wettability, tribology, and other areas [12-15].

The underlying physical mechanisms of LIPSS formation are still under debate. However, two different approaches can be found in the literature. The first one is the generalized scattering and interference model [16, 17] assuming that ripples are based on lithographic ablation after a modulated energy deposition, caused by an optical interference. The interference has often been attributed to the excitation of surface plasmon-polaritons (SPP) [18], since they can be easily addressed on a regularly corrugated surface [19, 20] with an

optical resonance wavelength slightly larger than their spatial period. This model explains very well structures consisting of long and almost parallel lines with periods close to the laser wavelength. But, it is not able to describe the dependence of the ripple period on the absorbed laser fluence and more complex features, such as multiple bifurcations [21]. The second approach to explain LIPSS formation is known as a self-organization model [21, 22]. It is very similar to models of surface structuring by ion beam sputtering and is based on the dynamics of energetic pulse interaction with the target material. By assuming that the absorbed laser energy leads to instabilities of the surface region due to softening and perturbation of crystal binding, it can explain a spontaneous formation of surface structures within the laser-modified area [21]. Moreover, the self-organization approach can also explain the recent observation of coherently connected LIPSS patterns in lines of individual spots with almost no spatial or temporal overlap [7].

In all experiments and all models, the laser polarization is a very important parameter during LIPSS formation, since the pattern morphology and orientation are controlled by the polarization of the laser-pulse electric field [4, 9, 11, 23]. The main focus of the present study lies on the investigation of the strictness of this polarization dependence of the ripples on a metal surface. For this purpose we followed the pulse-to-pulse evolution of the LIPSS formation when changing the polarization by 45° or 90° in the course of trains of picosecond-laser pulses. The experiments were performed both on a single spot as well as in line scans with 50% overlap between the adjacent spots with the laser radiation blocked during the target displacement. As a target we chose a polished surface of K890 cold work tool steel that is designed for high ductility, exhibiting a high capacity for plastic yield and high fatigue strength. Therefore, it is very suitable for tooling which requires high-edge stability. The surface patterning may be of importance for improvement in tribology approaches, where LIPSS can significantly reduce the friction [13].

2 Experimental

In all experiments, the fundamental (λ_0 = 1064 nm) of a Nd:YAG laser (Ekspla, Lithuania, PL2250-SH-TH) was focused onto the sample surface in nearly normal incidence under atmospheric pressure. The laser emits linearly polarized pulses of 30 ps duration (full width at half maximum; FWHM) at a maximum repetition rate of 50 Hz, which can be externally triggered. The laser beam was expanded by a 4× telescope to a diameter of 12 mm. In order to achieve a more circular spot, we placed a diaphragm with a diameter of 5 mm just behind the beam expander. A half-wave plate (HWP) in a rotation stage with an angular resolution of 0.3’ was placed just before the focusing objective (f = 120 mm), yielding a focal spot of 60 μm diameter. The pulse energy, measured by a pyroelectric detector (Gentec Electro-Optics, Inc., Canada, Solo with head QE12LP-H-MB) after the focusing objective, was set to 33 μJ during all our experiments, with a standard deviation, calculated from 500 pulses, of ±1.3 μJ.

As a target material we used cold work tool steel K890 (Böhler Edelstahl, Kapfenberg/Austria), based on powder metallurgy, consisting of 0.85% C, 0.55% Si, 0.40% Mn, 4.35% Cr, 2.80% Mo, 2.10% V, 2.55% W and 4.50% Co. After machining, the K890 specimen was quenched and triple tempered according to the steel producer specifications (T_A

= 1100°C, T_T = 500°C), achieving hardness of 64 HRC. Its surface was highly polished and ultrasonically cleaned in ethanol and distilled water before the processing.

The target (a rectangular cuboid with dimensions of 20×20×8 mm^3) was placed in a 3D positioning system, equipped with 3 linear stages (Eksma Optics, Lithuania) with 1 μm resolution. Here, the z direction is parallel with the excitation-pulse path, while the x axis is perpendicular to the z direction and parallel with an optical table. The y stage is tilted by about 5° in order to avoid the back reflection into the laser; so, the angle of incidence equals 85°. After processing, the samples were analyzed *ex-situ* by a scanning electron microscope (SEM; JSM-6500F) and by an atomic force microscope (AFM; Veeco, Dimension 3100).

3 Results

3.1 Surface morphology as a function of focal position

In a first set of experiments, we searched for the best focusing condition to obtain a spot with a most homogeneous ripple pattern. For this purpose, we moved the target along the z-axis around the focus plane (z = 0) within the range -3 mm ≤ z ≤ 3 mm. At each position, a constant number of pulses (N = 3) was applied onto a single spot. For each new spot we moved the sample for Δx = 150 μm to radiate a fresh patch of its surface. The images in Figs. 1(a)-1(f) represent typical surface structures at different positions around the focal plane, Figs. 1(g) -1(i) are magnifications from indicated spot areas. The double arrow under Fig. 1(g) shows the orientation of the pulse polarization.

When the surface is significantly out of the focus, at low fluence, only high-spatial frequency LIPSS (HSFL) [24] are generated with the orientation parallel to the light polarization and the period significantly below the laser wavelength, as clearly visible from Fig. 1(g), which is a magnification of Fig. 1(a). By approaching the surface to the focus position, the fluence increases and low-spatial frequency LIPSS (LSFL) with period around the pulse wavelength and orientation perpendicular to the pulse polarization [5, 6] appears in the center of the processed area, as visible from Figs. 1(b)-(d) and 1(h). However, if the surface is moved further towards the focal position, the local fluence of the central part of the beam exceeds the melting threshold of the material. This melting results in a blurring of the ripples structures, as is revealed from Figs. 1(e) and 1(f). Thus, on the target near the focus position three regions with different morphology [25], R1 - R3, exist [e.g., see Fig. 1(i)]. Region R3 exhibits HSFL with a period of around 200 nm and orientation parallel to the laser polarization; region R2 shows LSFL with period 0.97 μm and orientation perpendicular to the polarization, while region R1 corresponds to the region, where periodic LSFL is already blurred because of surface melting. It should be noted here, that we have carefully checked that R1 is not a fictive effect caused by the crater depth, defocusing the SEM measurements.

The three different regions, observed in Fig. 1, can be explained by a Gaussian beam profile, as schematically presented in Fig. 2(a). In this case, the regions R1-R3 appear due to different fluence thresholds F_{R1}, F_{R2} and F_{R3}. For a Gaussian spatial profile (diffraction), the fluence $F(z,r)$ as a function of focus position z and radius r is given by:

$$F(z,r) = F_0 \frac{w_0^2}{w^2(z)} \exp\left(-2r^2 / w^2(z)\right) \tag{1}$$

where F_0 is the peak fluence at $r = 0$ and $z = 0$, w_0 stands for the $1/e^2$ beam waist at the focus position (at $z = 0$) and beam radius $w(z)$ as a function of z depends on the laser wavelength λ:

$$w(z) = w_0 \sqrt{1 + \frac{z^2 \lambda^2}{\pi^2 w_0^4}}. \tag{2}$$

The correlation to the pulse energy is given by the integral over the profile and does not depend on the z-position:

$$E_{pulse} = F_0 \frac{w_0^2}{w^2(z)} \int_0^\infty \exp\left(-2r^2 / w^2(z)\right) \times 2\pi r dr = \frac{1}{2} \pi F_0 w_0^2 \tag{3}$$

The local fluence reaches the threshold for a specific process $F_{th} = \alpha F_0$ at radius r_{th}. Here, $0 \leq \alpha \leq 1$ is a dimensionless parameter. Combining (1) and (2), one can obtain the z-dependence of radius r_{th}, where the pulse intensity reaches the threshold F_{th}, as:

$$r_{th}(z) = w_0 \sqrt{\eta(z)}. \tag{4}$$

The dimensionless factor $\eta(z)$ in Eq. (4) is:

$$\eta(z) = \frac{1}{2} \frac{w^2(z)}{w_0^2} \ln\left(\frac{1}{\alpha} \frac{w_0^2}{w^2(z)}\right). \tag{5}$$

By fitting a circle to the edges of the regions R1-R3 in micrographs like those in Fig. 1, we measured the radii of these regions. They are presented as triangles (R1), circles (R2) and squares (R3) in Fig. 2(b). The solid curves in Fig. 2(b) show the fit of Eq. (4) to the measured threshold radii. As the fitting parameters we obtained the dimensionless coefficients for regions R1-R3: $\alpha_1 = 0.28$, $\alpha_2 = 0.42$, and $\alpha_3 = 0.67$. Additionally, the fit gives also the beam waist radius $w_0 = 30$ μm, which agrees fairly well with a nearly diffraction limited beam for our experimental parameters.

The border between regions R3 and R2 is very clear. Therefore, we obtained an excellent fit of the measured data for R2. Contrarily, it is difficult to determine the radius of region R1, since the edge between the molten region and LSFL is not very sharp. This results in a slight discrepancy between the measured data and the fit in the case of region R1. On the other hand, the significant deviation of the measured data from the fit in the case of R3 can be explained by the influence of the used diaphragm. Due to diffraction, only the central part of the beam approximates to a Gaussian profile, while at the edges of the beam, a diffraction pattern results in a deviation from the Gaussian distribution (e.g., see also Ref. [26]). Therefore, we used only the spots created less than 1.5 mm from the focal position for fitting the dimensionless coefficient α_1.

From the fitted dimensionless coefficients α the fluence thresholds can be calculated by putting the pulse energy E_{pulse} and beam waist radius w_0 into Eq. (3).

For the laser parameters in our experiments the peak fluence equals $F_0 = 2.4$ J/cm^2 and the ablation threshold fluence is between 0.02 J/cm^2 and 0.5 J/cm^2 [26-28]. From the fitted dimensionless coefficients α it can be therefore concluded that the HSFL appear for fluences 0.7 J/cm^2 < F_{R3} < 1.0 J/cm^2, while LSFL are induced for 1.0 J/cm^2 < F_{R2} < 1.6 J/cm^2. When local fluence exceeds 1.6 J/cm^2 the ripples become molten, as visible in region R1 in Fig. 1(i).

For all further experiments, we placed the sample 2 mm in front of the focus, where we obtained the LSFL in an area with diameter of 30 μm.

3.2 Irradiation of a single spot by multiple pulses with different polarizations

In a second set of experiments we investigated the evolution of LIPSS formation by multiple pulses (i.e., a train of laser pulses) on a single spot. Of particular interest, here, was the effect of superimposing pulses of different linear polarization. For each spot, the surface was first treated by N_i pulses of the linear polarization adjusted a parallel to the x-axis of the setup (θ_i = 0°). After an initial action of these pulses, we rotated the HWP and after several seconds the *same spot* was irradiated with N_s pulses having the electric-field vector rotated by an angle θ_s. Then, the sample surface was moved in x direction by Δx = 150 μm to a new position for the next irradiation.

In the first series of the experiments the electric-field vector for the secondary treatment was rotated by θ_s = 45° [Fig. 3(a)], while in the second series we set θ_s = 90° [Fig. 3(b)]. In both series we used the following combination of pulses: N_i+N_s = {3+0, 3+1, 3+2, 3+3, 0+3}. The results are presented in the SEM micrographs of Fig. 3. The double arrows on the right-hand-side of each micrograph show the polarization of pulses. Here, the gray, dashed double arrows show the polarization of pulses that were used for the *initial* treatment of the surface by N_i pulses (the gray numbers), while the polarization and the number N_s of pulses used for the *secondary* surface treatment is shown by the black double arrows and the black numbers, separately.

To obtain the surface-pattern period Λ and the direction of the ripple pattern we calculated the two-dimensional (2D) fast Fourier transform (FFT) from each SEM micrograph. The region that was used for the 2D FFT calculation is marked with the white dashed rectangles in the first row of Fig. 3. The 2D FFT image is shown on the right-hand-side of each SEM micrograph. In the scale, shown on the top, the wave number equals $k_0 = 2\pi/\lambda_0 = 5.90$ μm^{-1} (λ_0 = 1.064 μm is the wavelength of the excitation pulse). Figure 4 shows the quantitative analysis of all FFTs. The 1D-results in Fig. 4 were obtained from the 2D-FFTs by an angle averaging around the center. From the main peak that appears at $k = 1.1\ k_0$, the LIPSS period is calculated to be $\Lambda = 0.91\lambda_0 = 0.97$ μm.

The first–row panels in Fig. 3 show the surface after the initial treatment (N_i pulses with θ_i). The ripples appear perpendicular to the pulse polarization, as visible also from the 2D FFT

images. The second, third and fourth rows in Fig. 3 reveal that additional irradiation at polarization angle θ_s starts to change the surface morphology by introducing a new ripples orientation according to the new polarization. At only one additional pulse (N_s = 1), already, the initial ripples pattern is dramatically deleted. After $N_s = N_i$, the original ripples orientation has completely vanished, and only the new orientation is observed.

For diagonal secondary polarization [θ_s = 45°, Fig. 3(a)], already the first pulse rotates the ripples almost completely to the new orientation (perpendicular to the new polarization). After the second pulse, the initial pattern is fully erased. For perpendicular secondary polarization [θ_s = 90°, Fig. 3(b)], the pattern after the first pulse is very similar to the one previously obtained for circular polarization [9, 29], indicating a synchronous superposition of both orientations. This is also clearly visible from the corresponding, nearly perfect circular FFT result. Note here that only the LIPSS orientation is lost upon the first exposure by the secondary pulses, but its periodicity stays the same (i.e., Λ = 0.97 μm). By increasing the number of the secondary pulses, the spherical symmetry of the peaks distribution decreases and finally they appear strongly along the vertical axis.

Interestingly, the contrast of the surface morphology appears much stronger than in the case of the same number of θ_s-pulses without preceding θ_i = 0 irradiation (last row in Fig. 3). In fact, the contrast of (3+3) pulses of different polarization [e.g., the fourth row in Fig. 3(a)] seems to match that from (0+6) pulses of the same polarization shown in Fig. 5. In order to establish this effect of increased contrast undoubtedly, we analyzed the modulation patterns of the three spots (0+3) and (3+3) in Fig. 3(a) and (0+6) in Fig. 5 by AFM. The corresponding profiles along a horizontal trace across the center of the spots are shown in Fig. 6. As suggested from the SEM micrographs, the results clearly confirm that the ripples contrast depends *only* on the *total* exposure of all pulses. From the AFM scans spots we calculated also the peak-to-peak (PPA) median of these spots through their whole areas. If 3 pulses of the same polarization are applied into the same spot, the PPA median equals 57 nm. The PPA median for the spot, induced by 3+3 pulses of two different polarizations is twice as large and equals 120 nm. The very same result is measured for ripples induced by 6 pulses of the same polarization. For the particular case, shown in Fig. 5, we measured the PPA median to be 119 nm. This comparison reveals that a significantly clearer pattern is produced on a pre-treated surface, even by pulses of different polarization. This leads to very interesting conclusion, that the final *orientation* of the LIPSS depends on the polarization of the pulses that *finally* irradiate the surface, while the ripples *contrast* depends on the total exposure (i.e., total energy input) by *all* pulses, independently on their polarization.

3.3 Overlapping spots

In a third set of experiments we investigated the LIPSS formation in longer, "digital" line scans of overlapping individual spots. For each spot, the surface was initially treated with N_i = 3 horizontally (x) polarized (θ_i = 0°) pulses. Then, the laser was switched off and the sample was moved by Δx = 15 μm, i.e., by half of the LSFL spot diameter along the initial

polarization direction. After 15 steps, resulting in a 0.24-mm-long line scan, the sample was moved back to the initial starting position, the laser being switched off during this movement. After preparing several of such traces, a *secondary* surface treatment was performed in the same manner, superimposed on the initial traces but with the polarization rotated by $\theta_s = 45°$ [Fig. 7(a)] or $\theta_s = 90°$ [Fig. 7(b)], applying $N_s = \{1,2,3\}$ pulses per spot, each on a fresh initial trace.

Figure 7 shows SEM micrographs of the line scans. The 2D FFT images, embedded in each micrograph, were calculated as an average of two FFTs obtained from different areas of the line scan, as indicated by the white dashed rectangles in the upper panels. Figure 8 shows the quantitative analysis of FFT, obtained by an angle averaging of 2D FFT around the center.

The first row in Fig. 7 shows the part of the line scan that was only initially treated with $N_i = 3$ pulses (with $\theta_i = 0°$) per spot. As is visible from 2D FFT images, the ripples are oriented nearly perpendicular to the pulse polarization and the scan direction. The upper traces of the 1D FFT-analysis in Fig. 8 show a peak at $k = 1.1k_0$. This means that the ripples period equals $\Lambda = 0.97$ µm. It should be noted here, that a second peak appearing at $k = \pm 2.2k_0$ is an artifact of the FFT due to the deviation of the ripples from the harmonic function.

The second row in Fig. 7 presents the micrographs after a secondary exposure to $N_s = 1$ per spot. Like for the single-spot results in Section 3.2, in the case of $\theta_s = 90°$, a modified surface structure is obtained [Fig. 7(b)], similar to irradiation with circular polarization [9]. The influence of the secondary pulse is much less pronounced, for a rotation of only $\theta_s = 45°$ [Fig. 7(a)], where only a slight rotation of the pattern (less than 45°) is observed.

By increasing the number N_s of secondary pulses per spot (third and fourth rows in Fig. 7), re-orientation and contrast of the ripples increase with N_s. Interestingly, the ripples are less linear than in the initial treatment for lines, written only with the polarization at an angle to the scan direction (lowest row in Fig. 7).

The corresponding FFT-traces in Fig. 8 show, again, that the LIPSS period $\Lambda = 0.97$ µm does not change during the secondary treatment though the orientation follows the new polarization.

4 Discussion

The experiments on both individual spots as well as line scans give clear evidence that – at least for our target material of cold work tool steel – the orientation of LIPSS, formed by multiple pulses of different polarizations, is dominated by the polarization of the *last* incident pulses. Here, we are dealing with temporally well-separated irradiations, not with double-pulse irradiation with a separation within or close to any dynamic coherence times [30]. Further, the pre-structures are softly modulated, in contrast to sharp scratches which are known to override the polarization dependence of LIPSS orientation [31]. In fact, already one single pulse of a new, deviating polarization efficiently effaces a previously generated regular periodic surface modulation. This bears the potential of very interesting consequences for a better understanding of LIPSS formation with very short laser pulses on metal targets.

In the static lithographic model [17], resonant coupling of the incident laser light to SPPs on a regularly modulated surface play a key role [18]. This resonance is slightly red-shifted to the modulation periodicity for TM polarized light, i.e., the electrical field is perpendicular to the grooves. The corresponding intensity modulation of a (standing) SPP-wave, then, should amplify the existing regular surface corrugation [19, 20]. This coupling to an SPP is only possible for a TM wave, i.e. the electric field oscillating perpendicular to the corrugation grooves, because only there a component of the field may be parallel to a component of the wave vector. For TE polarization (electric field parallel to the grooves), there should be no such resonant coupling, since there is no electric field component in the propagation direction.

In our experiments, however, we demonstrate that LIPSS formation is possible on a regularly pre-corrugated surface with TE and 45° polarization (*secondary* irradiation). Against expectation, the structuring for TE irradiation is very strong without any SPP resonance. For 45° polarization SPP coupling might be possible, but with a resonance red-shifted by a factor of $\cos 45° = (1/2)\sqrt{2}$. Instead, the ripples preserve their periodicity and are only rotated according to the new electric field direction. These observations strongly defy the idea of a paramount key role of SPP resonances for the formation and properties of LIPSS. More likely, the results of [19, 20] indicate that SPP resonances may help laser-surface coupling but are not necessarily essential for LIPSS formation. On the other hand, the surprising observation that any pre-treatment increases the modulation efficiency, independent of the relative polarization (cf. Fig. 6), is not in good agreement with purely electromagnetic models [32, 33], which start from *random* roughness and then favor the enhancement of a pre-existing regular corrugation by additional irradiation. Both features, we observed, strongly require an important, autonomous contribution of the material response to structure formation, during relaxation after irradiation. This is in strong contradiction to the lithographic model [17].

In the dynamic self-organization model [21, 22], LIPSS formation does not depend explicitly on pre-structures which might be present on the surface. Energy input and structure formation are essentially decoupled: the energy input only drives the target surface into a state of thermal non-equilibrium (dynamic melting). The role of laser polarization comes into the play because it defines the preferential direction of energy flow after electron excitation [11]. LIPSS are then formed by non-linear dynamical relaxation from this non-equilibrium, with the orientation controlled by the dissipation and the feature size determined by the level of non-equilibrium, respectively. In this scenario, both the ripples re-orientation according to the *last* laser pulses and the conservation of the feature size are consistent. Even the observation of a better ripples contrast and aspect (cf. Fig. 6) after pre-irradiation (independent of polarization) is compatible with this model. Though here, too, positive feedback can increase the effect, just a persistence of the surface instability may be sufficient to support the structure formation. As was shown in a previous publication [34], the memory of a preceding excitation, i.e. residues of the non-equilibrium state, may last very long, much longer than the typical life-time of SPPs.

5 Conclusions

We have presented evidence that for LIPSS formation with multiple picosecond pulses on tool steel the *last* incident pulses determine the ripples orientation, even overriding previously formed structures. It should be noted, however, that this is not fully compatible with the observation that on dielectrics or semiconductors pre-structures like scratches can override the polarization dependence. This weak role of pre-formed structures makes the essential role of SPPs in LIPSS formation or other interference scenarios at least questionable. Instead, the experiments endorse the model of self-organized structure formation from a laser-induced thermal instability (dynamic melting).

Acknowledgements

The authors acknowledge the financial support from the state budget by the Slovenian Research Agency (Programmes No. P2-0392 and P2-0050).

References

[1] M. Birnbaum, Semiconductor Surface Damage Produced by Ruby Lasers, J. Appl. Phys., 36 (1965) 3688.

[2] F. Keilmann, Y.H. Bai, Periodic Surface-Structures Frozen into Co2 Laser-Melted Quartz, Appl. Phys. A, 29 (1982) 9-18.

[3] J. Kruger, W. Kautek, Femtosecond-pulse visible laser processing of transparent materials, Appl. Surf. Sci., 96-8 (1996) 430-438.

[4] J. Reif, F. Costache, M. Henyk, S.V. Pandelov, Ripples revisited: non-classical morphology at the bottom of femtosecond laser ablation craters in transparent dielectrics, Appl. Surf. Sci., 197 (2002) 891-895.

[5] A.Y. Vorobyev, V.S. Makin, C.L. Guo, Periodic ordering of random surface nanostructures induced by femtosecond laser pulses on metals, J. Appl. Phys., 101 (2007) 034903.

[6] J. Bonse, J. Kruger, S. Hohm, A. Rosenfeld, Femtosecond laser-induced periodic surface structures, J. Laser Appl., 24 (2012) 042006.

[7] J. Reif, C. Martens, S. Uhlig, M. Ratzke, O. Varlamova, S. Valette, S. Benayoun, On large area LIPSS coverage by multiple pulses, Appl. Surf. Sci., 336 (2015) 249-254.

[8] E. Rebollar, M. Castillejo, T.A. Ezquerra, Laser induced periodic surface structures on polymer films: From fundamentals to applications, Eur. Polym. J., 73 (2015) 162–174.

[9] S. Gräf, F.A. Muller, Polarisation-dependent generation of fs-laser induced periodic surface structures, Appl. Surf. Sci., 331 (2015) 150-155.

[10] J. Reif, O. Varlamova, F. Costache, Femtosecond laser induced nanostructure formation: self-organization control parameters, Appl. Phys. A, 92 (2008) 1019-1024.

[11] O. Varlamova, J. Reif, S. Varlamov, M. Bestehorn, The laser polarization as control parameter in the formation of laser-induced periodic surface structures: Comparison of numerical and experimental results, Appl. Surf. Sci., 257 (2011) 5465-5469.

[12] A.Y. Vorobyev, C.L. Guo, Direct femtosecond laser surface nano/microstructuring and its applications, Laser Photonics Rev, 7 (2013) 385-407.

[13] J. Bonse, R. Koter, M. Hartelt, D. Spaltmann, S. Pentzien, S. Hohm, A. Rosenfeld, J. Kruger, Femtosecond laser-induced periodic surface structures on steel and titanium alloy for tribological applications, Appl. Phys. A, 117 (2014) 103-110.

[14] M. Zupančič, M. Steinbücher, P. Gregorčič, I. Golobič, Enhanced pool-boiling heat transfer on laser-made hydrophobic/superhydrophilic polydimethylsiloxane-silica patterned surfaces, Appl. Therm. Eng., 91 (2015) 288-297.

[15] P. Bizi-bandoki, S. Valette, E. Audouard, S. Benayoun, Time dependency of the hydrophilicity and hydrophobicity of metallic alloys submitted to femtosecond laser irradiations, Appl. Surf. Sci., 273 (2013) 399

[16] J.E. Sipe, J.F. Young, J.S. Preston, H.M. VanDriel, Laser-Induced Periodic Surface-Structure .1. Theory, Phys. Rev. B, 27 (1983) 1141-1154.

[17] J. Bonse, A. Rosenfeld, J. Kruger, Implications of transient changes of optical and surface properties of solids during femtosecond laser pulse irradiation to the formation of laser-induced periodic surface structures, Appl. Surf. Sci., 257 (2011) 5420-5423.

[18] J. Bonse, A. Rosenfeld, J. Krüger, On the role of surface plasmon polaritons in the formation of laser-induced periodic surface structures upon irradiation of silicon by femtosecond laser pulses J. Appl. Phys., 106 (2009) 104910
[19] F. Garrelie, J. P. Colombier, F. Pigeon, S. Tonchev, N. Faure, M. Bounhalli, S. Reynaud, and O. Parriaux, Evidence of surface plasmon resonance in ultrafast laser-induced ripples, Opt. Express, 19 (2011) 9035
[20] K. Miyazaki, G. Miyaji, Nanograting formation through surface plasmon fields induced by femtosecond laser pulses, J. Appl. Phys., 114 (2013) 153108
[21] O. Varlamova, J. Reif, S. Varlamov, M. Bestehorn, Self-organized Surface Patterns Originating from Laser-Induced Instability, in: S. Sakabe, C. Lienau, R. Grunwald (Eds.) Progress in Nonlinear Nano-Optics, Springer International Publishing, 2015, pp. 3-29.
[22] O. Varlamova, F. Costache, J. Reif, M. Bestehorn, Self-organized pattern formation upon femtosecond laser ablation by circularly polarized light, Appl. Surf. Sci., 252(2006) 4702-4706.
[23] S. Höhm, A. Rosenfeld, J. Krüger, J. Bonse, Femtosecond laser-induced periodic surface structures on silica, J. Appl. Phys., 112 (2012) 014901.
[24] T.Q. Jia, H.X. Chen, M. Huang, F.L. Zhao, Q. Jr, R.X. Li, Z.Z. Xu, X.K. He, J. Zhang, H. Kuroda, Formation of nanogratings on the surface of a ZnSe crystal irradiated by femtosecond laser pulses, Phys. Rev. B, 72 (2005) 125429.
[25] M. Henyk, F. Costache, J. Reif, Femtosecond Laser Ablation from Sodium Chloride and Barium Fluoride, Appl. Surf. Sci., 186 (2002) 381-384.
[26] P.T. Mannion, J. Magee, E. Coyne, G.M. O'Connor, T.J. Glynn, The effect of damage accumulation behaviour on ablation thresholds and damage morphology in ultrafast laser micro-machining of common metals in air, Appl. Surf. Sci., 233 (2004) 275-287.
[27] B. Liu, W. Wang, G. Jiang, X. Mei, K. Wang, J. Wang, Formation of Porous Structure with Subspot Size under the Irradiation of Picosecond Laser Pulses, J. Nanomat., 2013 (2013) 301301.
[28] G. Raciukaitis, M. Brikas, P. Gecys, M. Gedvilas, Accumulation effects in laser ablation of metals with high-repetition rate lasers, Proc. SPIE, 7005 (2008) 70052L.
[29] O. Varlamova, F. Costache, M. Ratzke, J. Reif, Control parameters in pattern formation upon femtosecond laser ablation, Appl. Surf. Sci., 253 (2007) 7932-7936.
[30] S. Höhm, M. Herzlieb, A. Rosenfeld, J. Krüger, J. Bonse, Dynamics of the formation of laser-induced periodic surfacestructures (LIPSS) upon femtosecond two-color double-pulseirradiation of metals, semiconductors, and dielectrics, Appl. Surf. Sci., 374 (2016) 331–338.
[31] J. Reif, O.Varlamova, F. Costache, Femtosecond laser induced nanostructure formation: self organization control parameters, Appl. Phys. A, 92 (2008) 1019
[32] J.Z.P. Skolski, G.R.B.E. Römer, J.V. Obona, V. Ocelik, A.J. Huis in ‘t Veld and J.Th.M. De Hosson, Laser-induced periodic surface structures: Fingerprints of light localization, Phys. Rev. B, 85 (2012) 075320.
[33] J.Z.P. Skolski, G.R.B.E. Römer, J.V. Obona, and A.J. Huis in ‘t Veld, Modeling laser-induced periodic surface structures: Finite-difference time-domain feedback simulations., J. Appl. Phys., 115 (2014) 103102.
[34] J. Reif, O. Varlamova, M. Bounhalli, Tz. Arguirov, Long-Time Feedback in the Formation of Self-Organized Nanostructures upon Multipulse Femtosecond Laser Ablation,

pp. 446 - 456 in C.R.Phipps, ed.: International Symposium on High Power Laser Ablation 2010, AIP Conference Proceedings, 1278 (2010) AIP Melville, New York.

Figures

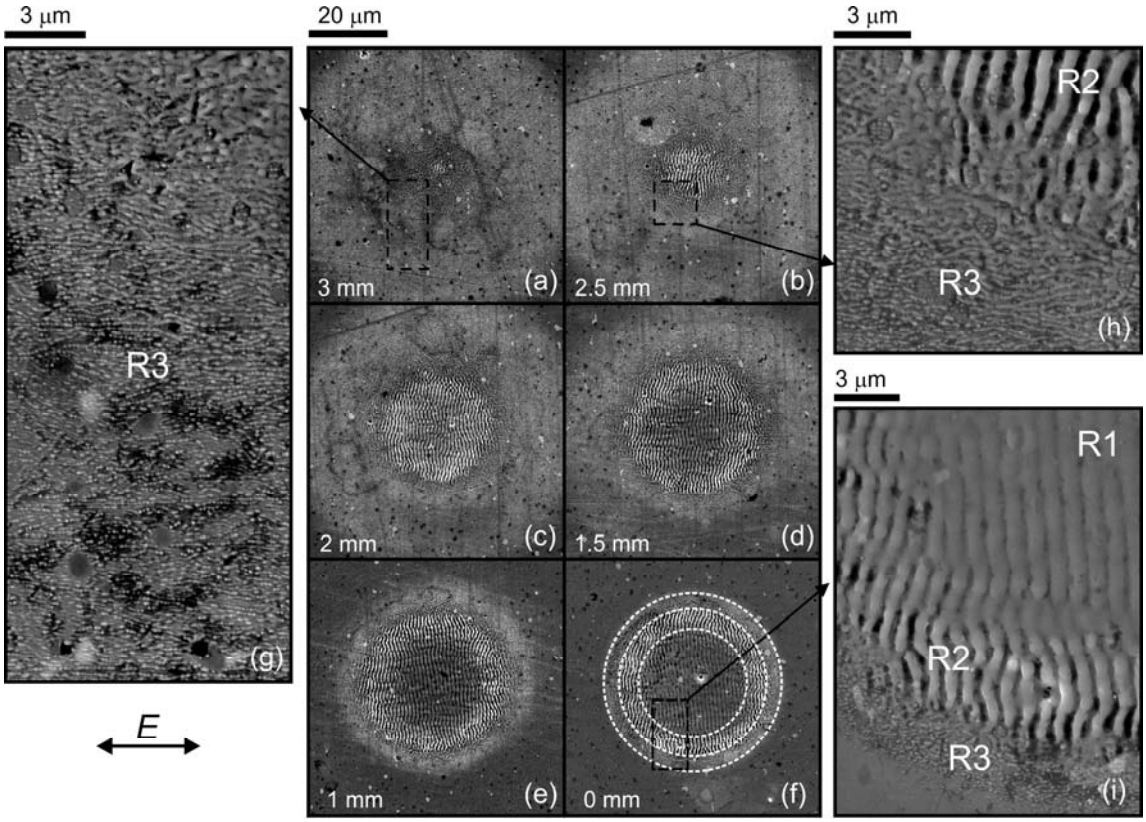

Fig. 1: SEM micrographs of surface morphology after irradiation by 3 pulses onto a single spot at different positions in front of the focal plane, listed below each image. Here, $z = 0$ corresponds to the focal plane. The black double arrow below (g) shows the polarization of the electric field (E). Three different regions are marked with R3 (HSFL), R2 (LSFL), and R1 (molten LSFL).

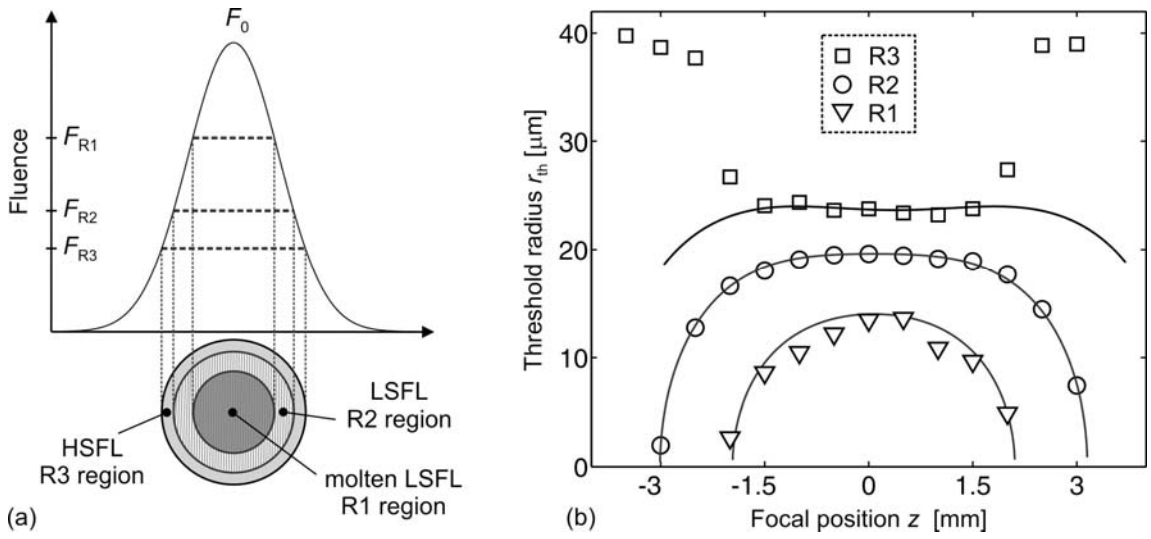

Fig. 2: (a) Different regions R1-R3 can be explained by different threshold fluences within a Gaussian beam profile. (b) Measured radii r_{th} of regions R3 (squares), R2 (circles), and R1 (triangles) as a function of focal position z. The solid curves show a fit [Eq. (4)] to the measured data.

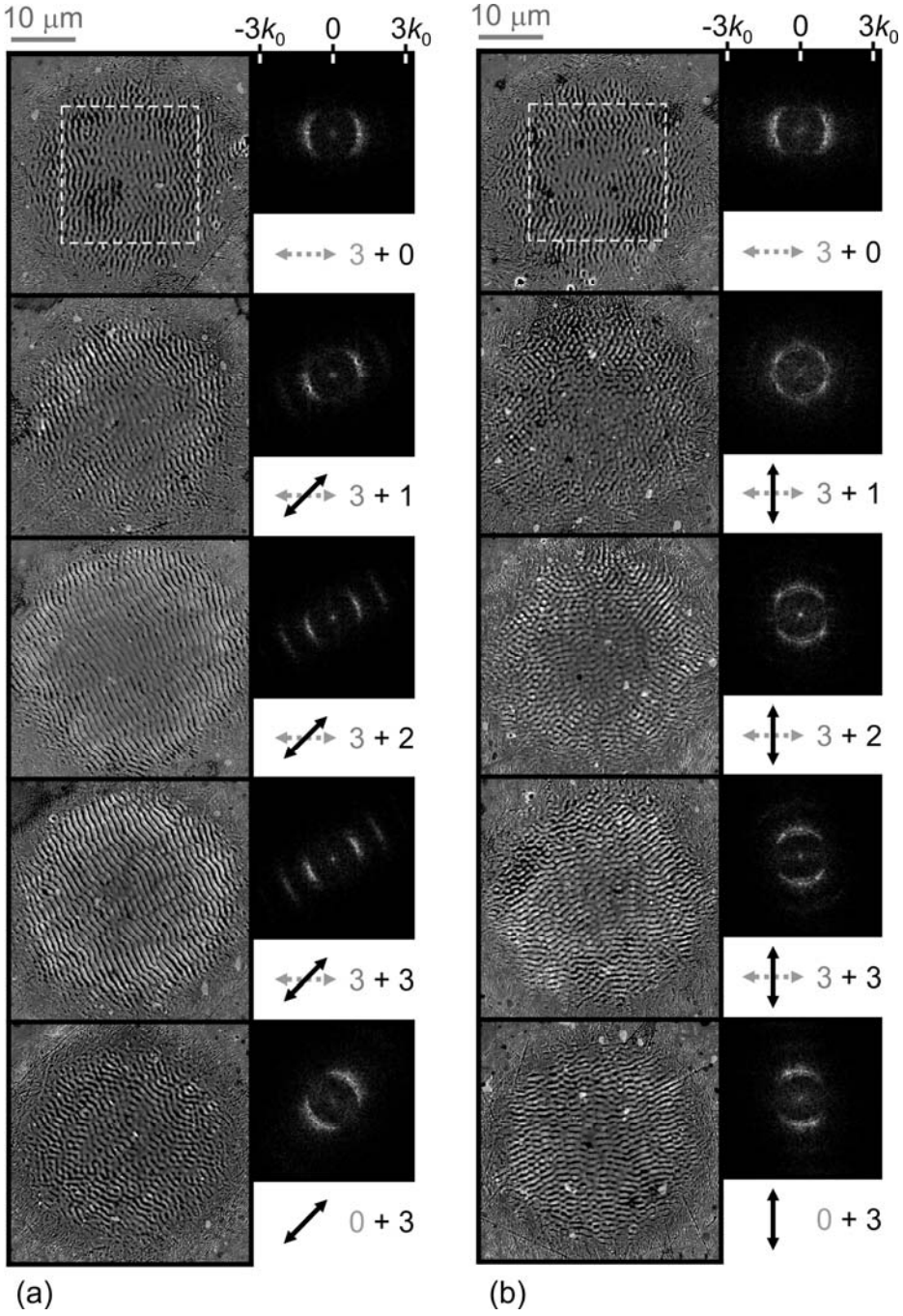

Fig. 3: SEM micrographs of single spots treated with 45-degree-polarized (a) and (b) 90-degree polarized secondary pulses. The 2D FFT images are shown on the right-hand side of each micrograph and k_0 = 5.90 μm^{-1}. The double arrows and numbers give the polarizations and pulse numbers (grey: θ_i, N_i; black: θ_s, N_s)

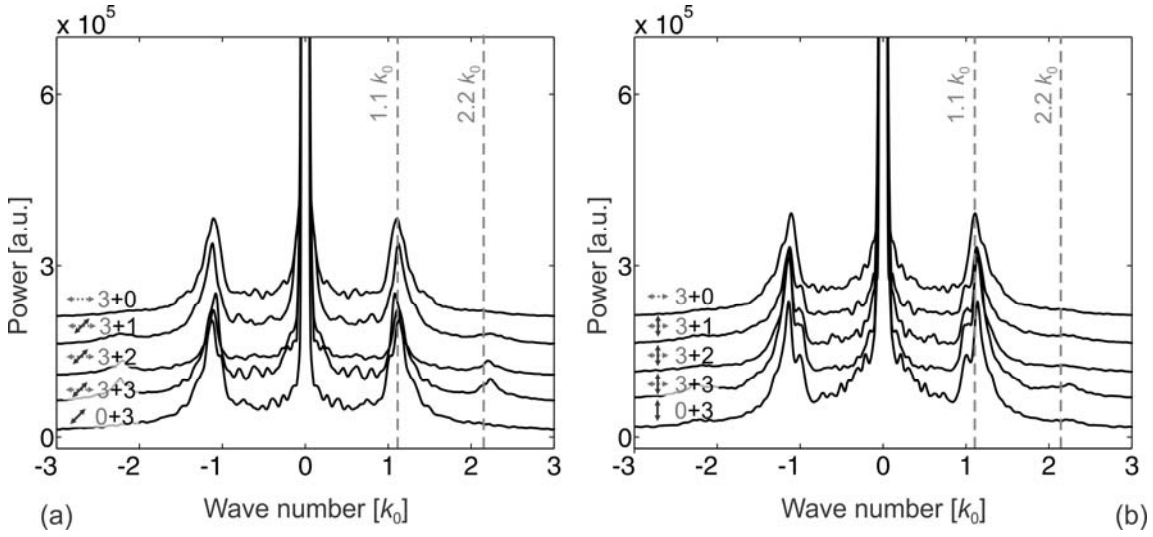

Fig. 4: The 1D FFT analysis of micrographs from Fig. 3 derived by angular integration [(a) for $\theta_s = 45°$and (b) for $\theta_s = 90°$]. The wave number k_0 equals 5.90 μm^{-1}. The second peaks at 2.2 k_0 that appear in some curves are an artifact of the FFT due to the deviation of the ripples from the harmonic function. (For clarity and facility of inspection, each trace is displayed with a different vertical offset.)

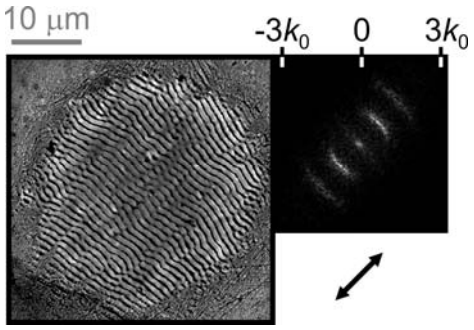

Fig. 5: SEM micrograph of a single spot induced by 6 pulses of polarization at 45°, as shown by the double arrow. The 2D FFT image is shown on the right-hand side and $k_0 = 5.90\ \mu m^{-1}$.

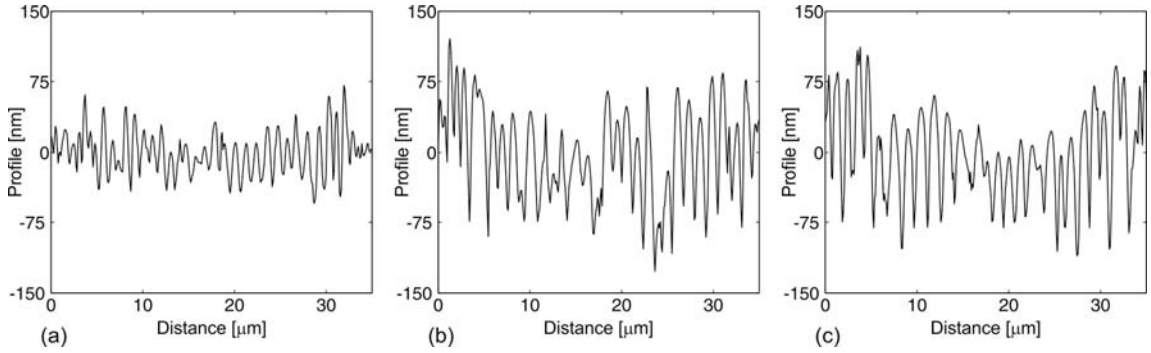

Fig. 6: AFM profiles in horizontal direction through the center of the following single spots: (a) induced by 3 pulses of horizontal polarization [the first row of Fig. 3(a)]; (b) induced by 3 pulses of horizontal polarization and additional 3 pulses having the polarization rotated by θ_s = 45° [the fourth row of Fig. 3(a)]; and (c) induced by 6 pulses of polarization at 45° (Fig. 5).

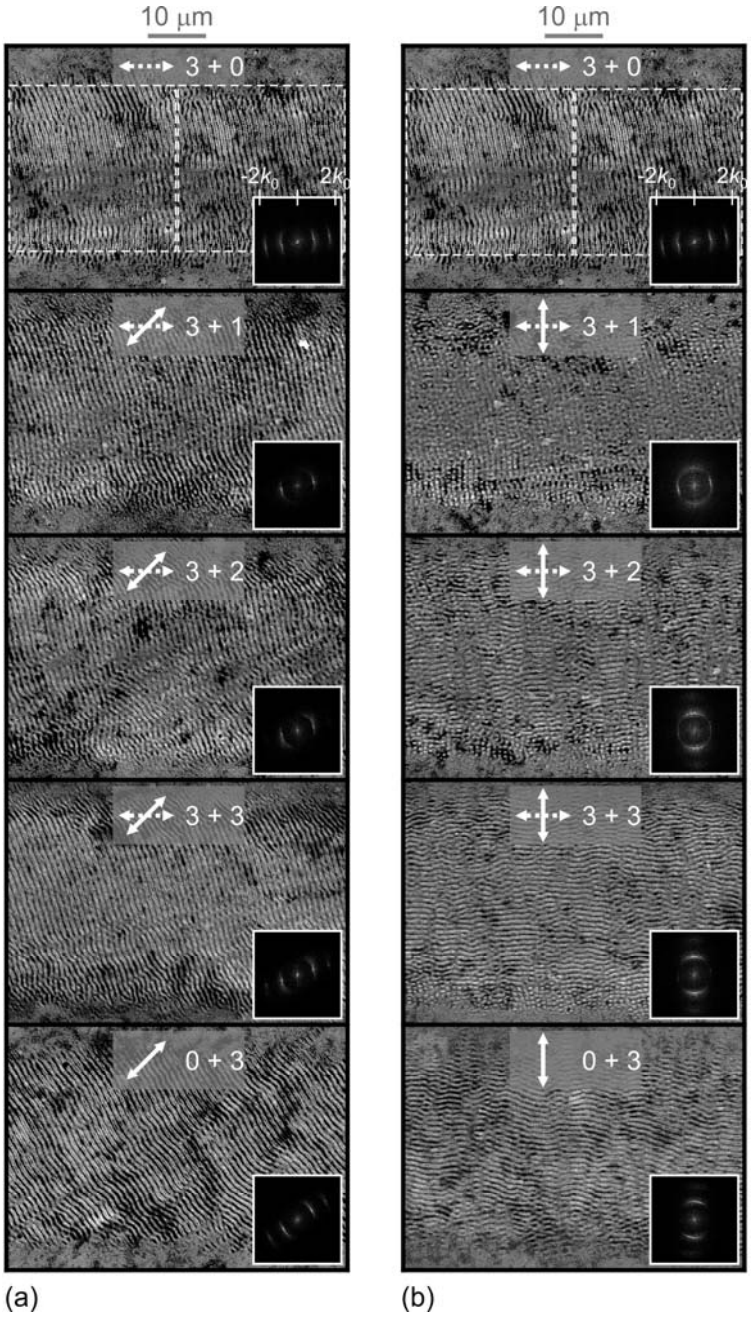

Fig. 7: SEM micrographs of the line scans. The traces were initially prepared by N_i = 3 horizontally polarized pulses per spot. The solid, white double arrows and the second numbers show the polarization and the N_s number of pulses per spot during the secondary surface treatment [(a) for θ_s = 45°and (b) for θ_s = 90°]. The 2D FFT is shown as an inset in each micrograph and k_0 = 5.90 μm^{-1}.

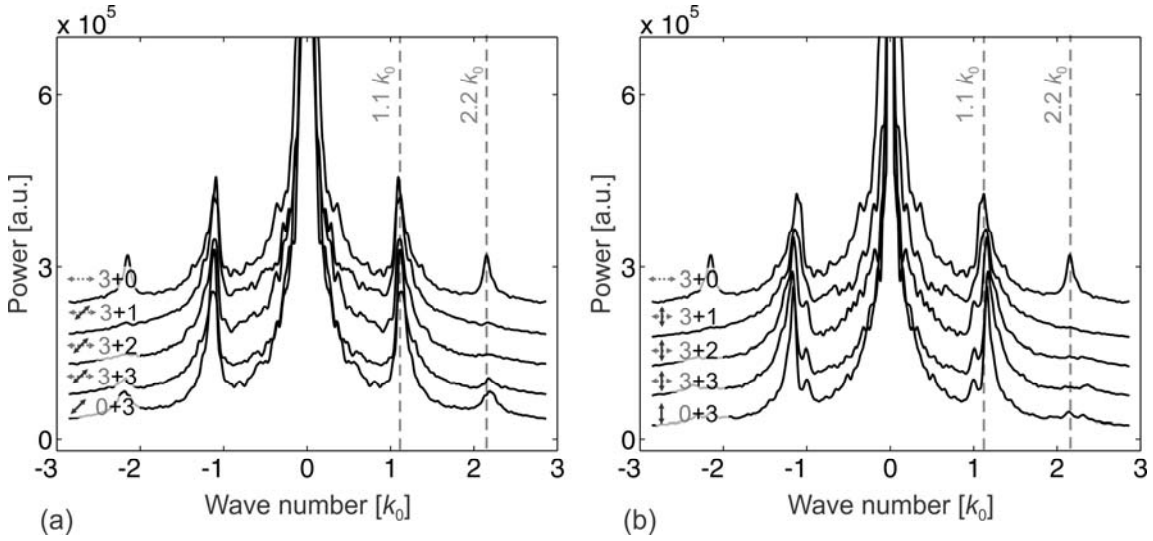

Fig. 8: FFT analysis of micrographs from Fig. 5 for (a) $\theta_s = 45°$ and (b) 90°, respectively. The wave number k_0 equals 5.90 μm^{-1}. The second peak at 2.2 k_0 is an artifact of the FFT due to the deviation of the ripples from the harmonic function. (For clarity and facility of inspection, each trace is displayed with a different vertical offset.)